One-Step Fabrication of Composite Hydrophobic Electrically Heated Graphene Surface for Anti-Icing

Mian Zhong *, Shichen Li, Hongyun Fan, Huazhong Zhang, Yong Jiang, Jinling Luo, Liang Yang *

Posted Date: 2 July 2024

doi: 10.20944/preprints202407.0123.v1

Keywords: LIG; Hydrophobic surface; electrically heated materials; one-step fabrication; contact angle

Article

One-Step Fabrication of Composite Hydrophobic Electrically Heated Graphene Surface for Anti-Icing

Mian Zhong[1*†], Shichen Li[1†], Hongyun Fan[1], Huazhong Zhang[1], Yong Jiang[2], Jinling Luo[3], Liang Yang[3*]

[1] Institute of Electronic and Electrical Engineering, Civil Aviation Flight University of China, Deyang 618307, China; mianzhong@cafuc.edu.cn (M.Z.); lscxy19990217@163.com (S.L.); 18731838513@163.com (H.F.); zhz_233@yeah.net (H.Z.);

[2] School of Mathematics and Physics, Southwest University of Science and Technology, Mianyang 621010, China; y_jiang@swust.edu.cn (Y.J.);

[3] Chongqing Institute of Green and Intelligent Technology, Chinese Academy of Sciences, Chongqing 400714, China; luojinling@cigit.ac.cn (J.L.); yangl@cigit.ac.cn (L.Y.)

* Correspondence: mianzhong@cafuc.edu.cn (M.Z.); yangl@cigit.ac.cn (L.Y.);

† These authors contributed equally to this work.

Abstract: Ice accumulation poses considerable challenges in transportation, notably in the domain of general aviation. The present study combines the strengths and limitations of conventional aircraft de-icing techniques with the emerging trend toward all-electric aircraft. The study aims to utilize laser-induced graphene (LIG) technology to create a multifunctional surface, seamlessly integrating hydrophobic properties with efficient electrical heating to mitigate surface icing effectively. We investigated the utilization of a 10.6 μm CO_2 laser for direct writing on polyimide (PI), a widely-used insulating encapsulation material. From the thermomechanical perspective, our initial analysis using COMSOL Multiphysics software revealed that when the laser power P exceeds 5 W, the PI substrate experience ablative damage. The experimental results show that when P ≤ 5W, an increase in power has a positive impact on the quality, surface porosity, roughness reduction, line-spacing reduction, and water contact-angle enhancement of the graphene. Conversely, when P > 5 W, higher power negatively affects both the substrate and the graphene structure by inducing excessive ablation. However, it influences the graphene line height positively and is consistent with overall experimental-simulation congruence. Furthermore, the incorporation of high-quality graphene resulted in a surface that exhibited higher contact angles (CA > 120°), lower energy consumption, and higher heating efficiency compared to the use of traditional electrically heated materials for anti-icing applications. The potential applications of this one-step fabrication method extend across various industries, particularly aviation, marine engineering, and other ice-prone domains. Moreover, the method has extensive prospects for addressing pivotal challenges associated with ice formation and serves an innovative and efficient anti-icing technology.

Keywords: LIG; Hydrophobic surface; electrically heated materials; one-step fabrication; contact angle

1. Introduction

The prevention of icing has been identified as a crucial meteorological factor for ensuring the safe operation of aircraft [1]. To prevent severe icing during high-altitude aircraft operations, two types of anti-icing methods are employed: active anti-icing and passive anti-icing. Active de-icing systems are widely utilized [2], but they have limitations, including the incomplete removal of ice, environmental pollution, and high energy consumption. It has therefore been necessary to develop new deicing technologies, and this has led to the emergence of passive deicing technologies. These technologies have focused primarily on superhydrophobic surface designs that have originated from research on the science of material surfaces based on bionics [3]. This approach mainly enhances the wettability of materials by constructing micro-rough structures or surfaces with low surface energies

 doi:10.20944/preprints202407.0123.v1

to improve the water contact angle and reduce water/ice adhesion, thereby achieving delayed icing prevention and anti-icing effects [4]. Its unique wettability properties and large liquid contact angle make this surface technology exceptional, with features like self-cleaning [5], ice resistance [6], and antifreeze capabilities [7]. This technology has gradually matured while promoting the advancement of deicing and anti-icing technology.

Numerous researchers have employed various methodologies for fabricating superhydrophobic surfaces [8,9]. However, practical applications of such surfaces in industrial settings remain unsatisfactory because of their susceptibility to external forces, the inadequate adhesion of hydrophobic structures, the propensity for coating detachment, the weak corrosion resistance of micro-rough structures, complex preparation processes, and limited application scenarios. These drawbacks have significantly hindered the integration of superhydrophobic surfaces into real-life applications. Nevertheless, with advancements in laser technology, research teams have been working to design and prepare more-sophisticated micro–nano structures and to achieve greater stability of surface modifications [10]. By harnessing the advantages offered by laser processing—such as minimal thermal effects, high-precision processing capabilities, non-contact procedures, and simple repeatability, while incorporating graphene [11], this approach has emerged as a primary direction for advancing micro–nano superhydrophobic surface processing.

A comprehensive analysis of current anti-icing technologies reveals that, while active anti-icing technology is relatively mature, it still faces challenges such as high energy consumption and pollution. On the other hand, passive anti-icing technologies provide good anti-icing effectiveness, although they lack sustainable performance in use and involve complex preparation processes. The rapid development of the aviation industry has also increased the demand for low energy consumption, high stability, sustainability, and large-scale preparation in deicing technologies. Consequently, researchers have shifted away from traditional single deicing approaches to adopting composite deicing strategies. This entails the creation of a functional surface on an aircraft that combines hydrophobicity with micro–nano structures to provide effective ice prevention along with thermal deicing capabilities [12–15].

Recently, the coupling of superhydrophobic properties with an efficient electric-heating function has attracted significant attention from numerous research teams [16–18] as an advanced anti-icing/deicing technology. The utilization of materials for efficient electric heating to provide thermal deicing not only reduces energy consumption but also enhances the effectiveness of anti-icing measures, thereby compensating for the limitations of active anti-icing technology. Currently, a number of research teams have made significant progress in this field. For example, the morphology and composition of a graphene surface can be modified by adjusting laser parameters such as radiant energy [19], amount of defocusing [20], scanning frequency, the design and optimization of the laser-scanning pattern, and the modification of the substrate materials or graphene products [21], among others. The application of these technologies by certain research groups in the design and investigation of graphene-based superhydrophobic surfaces has yielded remarkable superhydrophobic effects, further enhancing their potential applications for anti-icing. In particular, Tour's team [22], who pioneered the discovery of laser-induced graphene (LIG) technology, achieved distinct wetting characteristics on polyimide (PI) substrates by using a 9.3 μm CO_2 laser to alter the surface in environments with controlled atmospheres. Their results demonstrated that laser irradiation in air or in an O_2 environment produced graphene surfaces with superhydrophilic properties. Conversely, the same surface exhibited superhydrophobicity when exposed to atmospheres of Ar or H_2, resulting in water contact angles of 152° and 157°, respectively. Moreover, in an SF_6 atmosphere, the contact angle could even exceed 160°. This research has played a pivotal role in expanding the scope of applications for LIG; however, it has also revealed a critical challenge: that of attaining a superhydrophobic graphene surface in ambient air.

A novel solution to this crucial issue was proposed by other research teams. For example, the Collin research team successfully achieved the transformation of a graphene surface from hydrophilic to hydrophobic in air using a CO_2 laser [23]. They accomplished this by implementing grid-like laser-scanning patterns and precise adjustments of the laser power. Their test results demonstrated that

 doi:10.20944/preprints202407.0123.v1

the resulting surfaces had remarkable durability and sustained corrosion resistance, with a maximum contact angle of 170° and a rolling angle of 0.61° ± 0.3°, and that membrane distillation and desalination were economically feasible. Their study thus established a robust foundation for the subsequent efficient, stable, and cost-effective preparation of superhydrophobic graphene surfaces for anti-icing applications. An additional novel method involves the manipulation of the microstructure of the graphene surface by varying the number of irradiation points per inch within the processing pattern [24]. The outcome of this process led to a morphological transformation from robust petal structures to graphene forests, accompanied by alterations in surface roughness. Ultimately, this resulted in the formation of a superhydrophobic graphene surface with a contact angle exceeding 150°. A hydrophobic graphene structure also can be achieved by adjusting the scanning speed of an ultraviolet laser precisely [25]. Further, experimental results using the Joule-heating method have validated its potential application to aircraft deicing. Furthermore, other investigators have employed a simple annealing treatment to achieve precise control of the surface energy of graphene and facilitate the attainment of a superhydrophobic surface. A DC bias voltage was subsequently utilized to modulate wetting characteristics of the surface effectively and enable directional water transport [26].

Based on the advantages of a small-diameter laser spot and meticulously designed patterns, several research teams have successfully manipulated the macro-structure of graphene through precise adjustments and modifications to obtain bionic-pattern designs. For instance, a bionic structure [27] inspired by the lotus leaf exhibited an impressive static water contact angle of 163.5° and a minimal water rolling angle of 3.7°. A taro-leaf structure [28] achieved a broad, static, water-contact angle ranging from 130° to 151°, accompanied by a small water rolling angle, between 3.3° and 4.8°. The bionic structure inspired by natural oxalis [29] attained an exceptional static water contact angle (WCA) of approximately 153.5° ± 0.6°, along with a remarkably low water rolling angle of approximately 2.5° ± 0.5°, demonstrating superhydrophobic stability lasting up to 100 days (with WCA ≈ 150°). These bionic-pattern surfaces exhibit superhydrophobic properties with enhanced stability, compared to traditional materials. Furthermore, they demonstrate superior anti-icing potential compared to conventional silicone rubber or fluorosilane superhydrophobic surfaces [30,31].

In summary, graphene surfaces with micro/nano structures represent novel hydrophobic, deicing, and anti-icing materials[32,33]. The LIG technology offers an efficient and reliable technical approach for the preparation of innovative anti-icing surfaces. Despite the numerous studies performed over the past decade on the impact of various laser parameters on the microstructure of graphene—which have led to the successful development of surfaces with superhydrophobic and anti-icing properties—there remains a lack of comprehensive exploration regarding the relationship between laser parameters and microstructure regulation[34]. It is therefore essential to conduct a systematic analysis and comprehensive summary of the effects of the laser parameters on these properties by examining their exclusive impacts on the outcomes. This ultimately necessitates intricate exploratory steps involving combinations of parameters during the preparation process. By further exploring the intrinsic characteristics of LIG, we thus expect to enhance its application value while leveraging its unique advantages toward achieving greater economic efficiency and environmental friendliness.

2. Materials and Methods

2.1 Material and Characterization Equipment

The original material we used to produce LIG was a 125-μm-thick PI film purchased from a commercial corporation (Shenzhen Jihongda Plastic Products Co., Ltd., Shenzhen, CHN). We generated the LIG in ambient air using a SynRAD-P150 CO_2 laser (Synrad, Inc., Bedford, MA, USA) with a wavelength of 10.6 μm and a pulse width of 100 ns. We characterized the surface morphology of the LIG using a Thermo Scientific Helios 5 CX-type focused-ion-beam scanning electron microscope (FIB–SEM, Thermo Fisher Scientific Inc., USA). We measured the height of the two-

 doi:10.20944/preprints202407.0123.v1

dimensional LIG plane using laser-scanning confocal microscopy (LSCM, Leika Microsystems, Germany). We determined the positions of the Raman spectral peaks due to PI and LIG using a Renishaw inVia confocal Micro Raman spectrometer (Raman, Gloucestershire, UK). We analyzed the atomic compositions of PI and LIG using FEI ESCALAB Xi+ XPS(Thermo Fisher Scientific Inc., USA). We employed a contact-angle tester (Kruss Scientific Instruments Co., Ltd, Germany) to perform three measurements of the contact angle for each sample. We utilized an RTS-8 four-probe tester (Guangzhou Four-probe Technology Instrument Co. Ltd, China) to assess the resistance of the graphene surface. We employed a DP800 programmable direct-current source (RIGOL Technologies, Inc., China) to supply static voltages. We used an iX650 infrared thermal-imaging device (Fluke Corporation, USA) to observe and record changes in both the surface temperature of the graphene and the steady-state temperature under different power conditions.

2.2 Experimental Processing

We first cleaned the PI film using an ultrasonic machine with distilled water and then dried it in a constant-temperature dryer. We then positioned the PI film at the focal point of the laser lens for irradiation in a line-by-line manner. We utilized a digital oscillator to control the laser beam, and we manipulated the laser parameters using Marking Mate V2.7d-3.22 software. During the LIG preparation process, we employed the following laser parameters: scanning speed of 100 mm/s, laser power ranging from 3 W to 7 W (in intervals of 1 W), laser-pulse frequency of 20 kHz, aperture lens focused at 95.5 mm, and a laser-beam diameter of 0.1 mm. This investigation focused on the impact of varying the laser power on the evolution of the surface morphology and the anti-icing effect of the LIG while keeping other parameters constant, as shown in Figure 1.

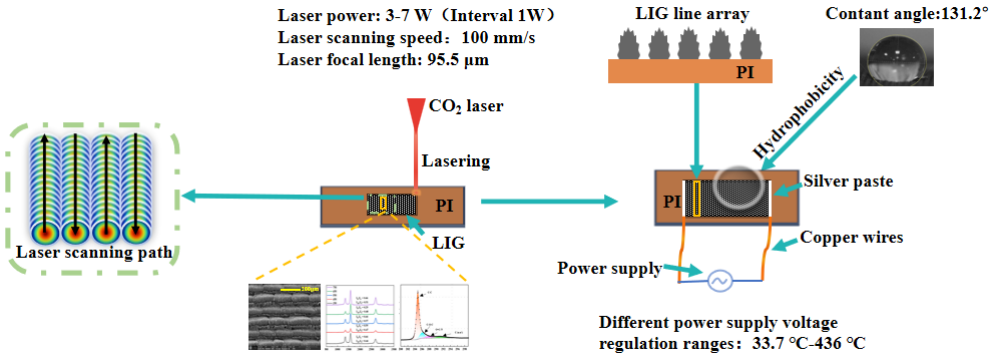

Figure 1 LIG preparation process.

3. Results and discussion

3.1 Surface Morphology of LIG

The formation of graphene on the surface of the PI film is illustrated in Figure 2. A complete layer of graphene is formed; however, we observed a noticeable non-uniformity of the obtained graphene surface when the laser power was set to 3 W. The inherent blackness of the graphene surface intensifies progressively as the power is increased, and certain regions at the laser's operational boundary become partially detached when the laser power exceeds 5 W. Significant burning and blacking are also evident on the backside of the film, which we attribute to excessive heat accumulation caused by the high laser power. This thermal effect not only induces deformation of the film but also compromises the integrity of the graphene.

 doi:10.20944/preprints202407.0123.v1

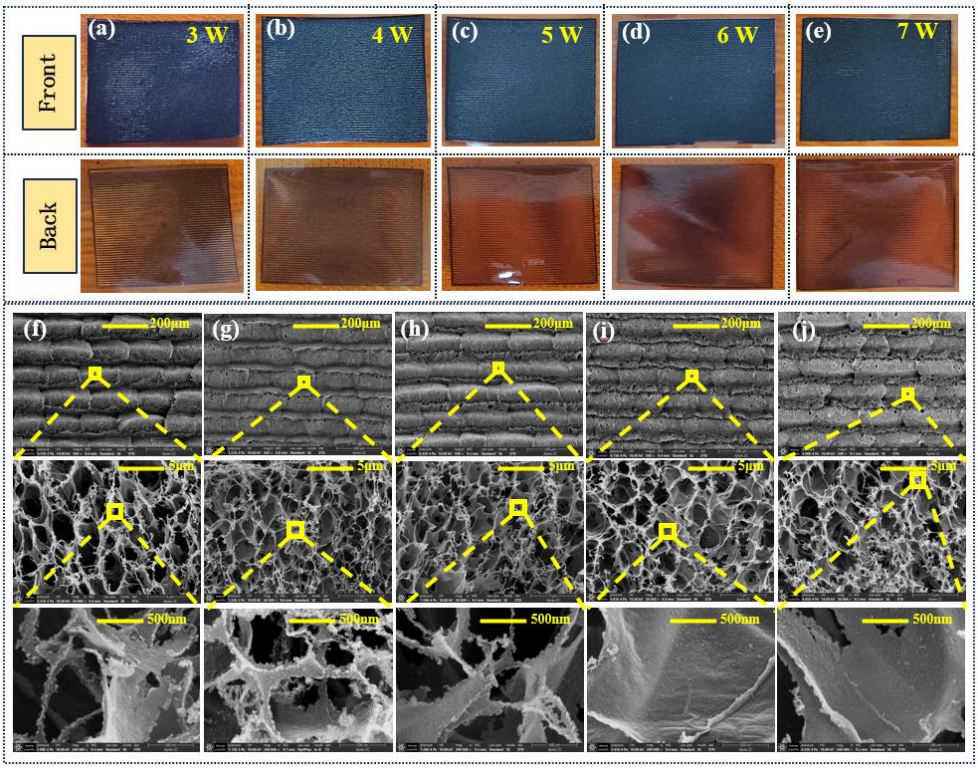

Figure 2 (a)–(e) LIG products on the PI film. (f)–(j) SEM images of the LIG surfaces formed at different powers.

To investigate the impact of laser power on the microstructure of the LIG further, we performed a comprehensive analysis of the surface microstructure using FIB–SEM at both micro and nano scales. The surface morphologies of the LIG over the power range from 3 W to 7 W are presented in the SEM images shown in Figure 2. For laser powers less than 3 W, the presence of semi-cylindrical convex structures—which correspond to the laser-scanning trajectory—and an overlapping "sand-ridge structure" on the graphene surface appear clearly at a scale of 200 μm. We attribute these features to an insufficient laser power, which resulted in inadequate heat accumulation on the PI surface and led to the generation of graphene of non-uniform quality and with an inconsistent thickness. Moreover, we observed a dense distribution of pore structures on the surface. When the laser power reached 4 W, the overlap phenomenon gradually diminished, resulting in a smoother surface with densely distributed pores between the laser tracks and large pores that appeared sparsely at the edge of the graphene line array. The prominence of laser-scanning marks was enhanced for surfaces prepared with a laser power exceeding 5 W, while the sparse, overlapping "sand-ridge structures" reappeared at laser powers of 6 W and 7 W. Thus, the decomposition of the PI was more pronounced at the increased laser powers, resulting in a gradual shift of defect-like macroporous structures from the gaps between laser trajectories toward their centers.

We analyzed further the impact of laser power on the evolution of the LIG surface morphology , in conjunction with the test results obtained at 5 μm and 500 nm. We observed the presence of filamentous materials on the graphene surface when the laser power was less than 5 W, while nanoscale particles of PI that were incompletely decomposed were detected on the surface and at the boundaries of semi-closed pores, in addition to filamentous structures. However, the LIG surface underwent a gradual transformation from a flocculent structure to a bramble structure when the laser power exceeded 5W, and this was accompanied by a transition of the pore morphology from a fully open state to an entirely exploded state . Moreover, the nanoscale PI particles located at the peripheries of the pores gradually vanished, indicating complete degradation of the PI film. These SEM test results are consistent with the findings derived from simulation analysis [32].

We investigated quantitatively the mechanism and effect of the laser power by processing and analyzing the two-dimensional (2D) height diagram of the graphene plane obtained from the LSCM

 doi:10.20944/preprints202407.0123.v1

measurements. The 2D LIG height diagrams corresponding to power levels ranging from 3 W to 7 W are shown in Figure 3(a)–(e). We processed the 2D height diagram using Gwyddion-2.43 software to obtain measurements of the line roughness and surface roughness for five different surface structures. We obtained the line-roughness measurements from random interceptions perpendicular to the direction of the graphene line array, as depicted in Figure 3(f) and (g). There is a striking similarity in the patterns of the variations in linear roughness and surface roughness. From a macroscopic perspective, the consistent variation trends observed in both the local and overall data provide evidence of a relatively comprehensive periodic structure with the surface. From a microscopic perspective, Figure 3(f) and (g) exhibit an X-axisymmetric relationship between the linear roughness and surface roughness variations of the graphene surface, as well as with the pore-size variations. At a laser power of 5 W, the LIG displays a surface microstructure with a smaller pore size (1.84 μm) and larger surface roughness (51.0 μm), which simultaneously enhance its hydrophobic properties.

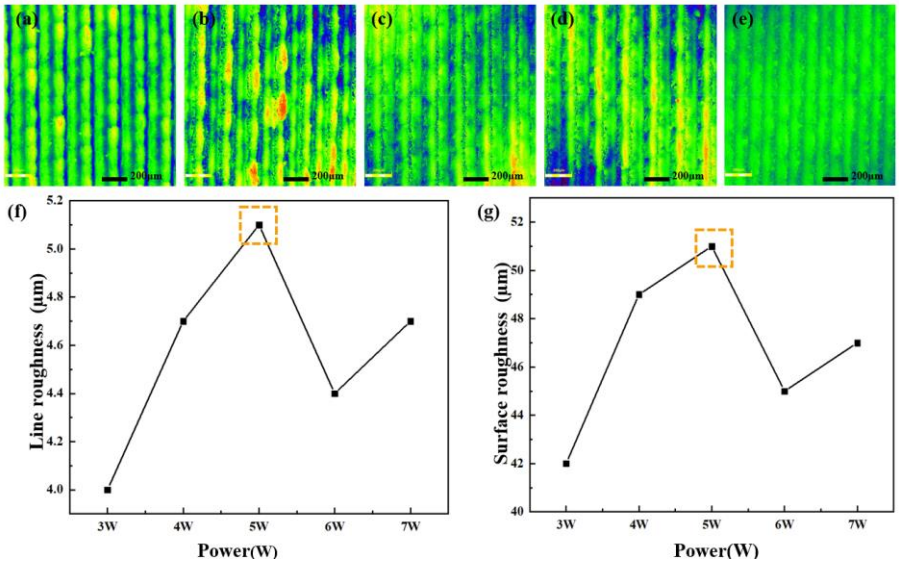

Figure 3 The surface of the LIG. (a)–(e) Two-dimensional height diagram. (f) Line roughness. (g) Surface roughness.

3. 2 Composition Analysis of the LIG

To investigate further the impact of laser power on the elemental composition of the graphene, we employed an X-ray photoelectron spectrometer with an aluminum target to analyze the total XPS spectrum and the changes in elemental C/N/O content both for the original PI film and for graphene fabricated using different laser powers, as illustrated in Figure 4(a) and (b). The C1s peak increased significantly upon the induction of graphene formation from the PI, as shown in Figure 4(a), and we observed no significant variations in peak height for the different laser powers. The N1s peak remained relatively unchanged, whereas the O1s peak exhibited a notable decrease. The analysis shown in Figure 4(b) reveals that laser irradiation applied to a PI film results in an increased carbon content within the graphene, while the levels of elemental nitrogen/oxygen are reduced compared to their initial state. The carbon content increased gradually from 82.64%, for the original PI, to 95.14% when the laser power reached 5 W, with a tendency toward saturation at approximately 95.5%. Moreover, a continuous increase in laser power leads to a significant decrease in elemental oxygen/nitrogen on the surface. We attribute this phenomenon to the photothermal-decomposition reactions that occur at the PI surface, which results in the discharge of N and O into the surrounding environment.

Preprints.org (www.preprints.org) | NOT PEER-REVIEWED | Posted: 2 July 2024 doi:10.20944/preprints202407.0123.v1

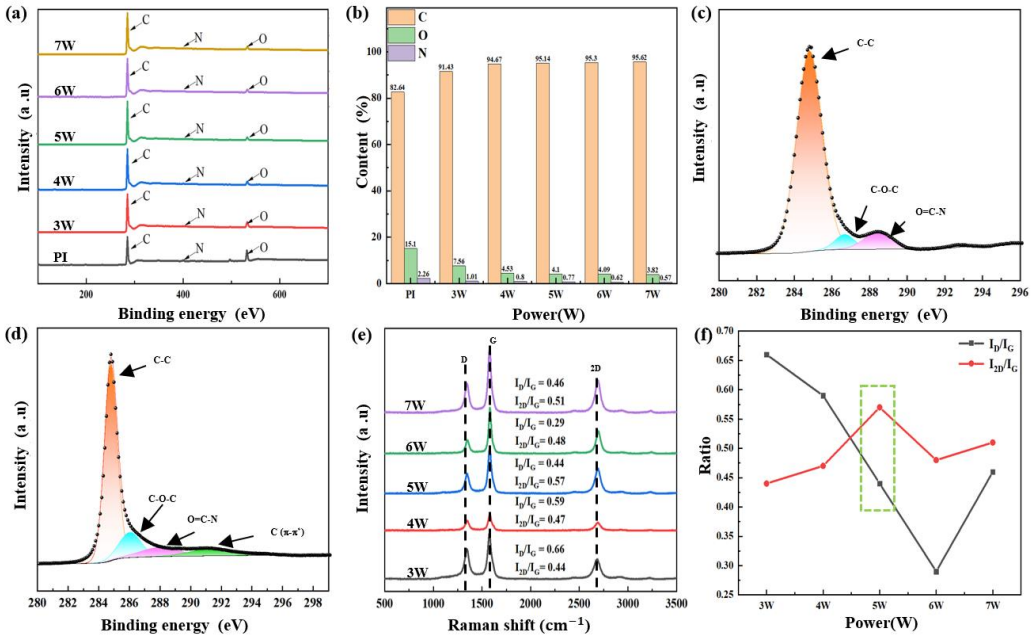

Figure 4 LIG characterization. (a) Total XPS spectrum. (b) Elemental C/N/O content. (c) C1s spectra of PI films. (d) C1s spectra of graphene surface prepared at 5 W. (e) Raman spectrum test results. (f) Trends of the I_D/I_G and I_{2D}/I_G ratios.

To investigate the atomic-structure transformations of the PI surface further during the photothermal-decomposition process, Figure 4(c) and (d) present the C1s spectral analysis results for the graphene surface prepared at a laser power of 5W. The XPS spectrum in Figure 4(c) clearly reveals the presence of distinct C–C bonds (at approximately 284.8eV), C–O–C bonds (around 286.0eV, representing phenyl ether bonds), and O=C–N bonds (about 288.1eV) in the original state of the PI. Furthermore, as shown in Figure 4(d), the PI film undergoes decomposition upon laser irradiation and transforms into graphene. The elevated temperatures facilitate the breakdown of the O=C–N bonds within the original structure, releasing gaseous elemental nitrogen into the surrounding environment during thermal decomposition. This consequently leads to a decrease in the peak strength for the O=C–N bond within the graphene. The peak strength of the C–O–C bonds tend to increase; however, there is an overall tendency for a reduction in oxygen content due to the partial release of gaseous oxygen atoms when the O=C–N bonds are broken. The remaining oxygen atoms then recombine with carbon atoms on the surface of the graphene [35]. We also observed that π–π* bonds were present on the graphene.

We employed Raman spectroscopy, with an excitation wavelength of 532 nm, to analyze the spectrum of the LIG on the surface over the wavelength range 500 cm^{-1} to 3500 cm^{-1}, as shown in Figure 4(e). The LIG surface exhibited three prominent peaks characteristic of graphene: Peak D (at approximately 1345 cm^{-1}), peak G (around 1572 cm^{-1}), and peak 2D (around 2687 cm^{-1}). Peak D arises from defects present in the graphene structure, peak G originates from the in-plane vibrations of hybrid sp2 carbon atoms, and peak 2D corresponds to double-resonance Raman scattering, which is often utilized to describe interlayer stacking between C atoms or the multilayer structure of graphene [36].

We measured the changes in the intensity ratios I_D/I_G and I_{2D}/I_G ratios to investigate the impact of the laser power on structural defects in the graphene and the quality of the generated graphene, as shown in Figure 4(f). In particular, the I_D/I_G ratio serves as a useful indicator for characterizing the graphene defects and evaluating the quality of graphene production. A higher I_D/I_G value indicates more defects in the graphene structure. As the laser power is increased from 3 W to 6 W, the I_D/I_G ratio decreases from 0.66 to 0.29. We attribute this to the enhanced decomposition of the PI that results from the increased laser power, which thereby facilitates an improvement in graphene quality. However, when the laser power exceeds 6W, we observed an elevated I_D/I_G ratio due to excessive

 doi:10.20944/preprints202407.0123.v1

heat accumulation, which induces gasification and generates structural defects in the graphene. In addition, the I_{2D}/I_G value serves as a distinctive characteristic of the multilayered graphene structure. As the laser power is increased to 5 W, the I_{2D}/I_G ratio rises from 0.44 to 0.57, gradually highlighting the distinguishing features of the multilayer graphene structure. However, the I_{2D}/I_G ratio decreases beyond a laser power of 5 W. The increased power has a detrimental impact on graphene generation and on the fabrication of micro and nano structures. This analysis of the changes in the I_D/I_G and I_{2D}/I_G ratios reveals that a laser power of 5 W ensures the production of a high-quality, multilayered graphene structure.

3.3 Hydrophobicity of the LIG

We analyzed quantitatively the vertical dimension (line height), horizontal dimension (line width), and inter-line distance (line spacing) of the two-dimensional graphene height diagram. The trend obtained by combining the SEM testing and the two-dimensional height diagram of graphene is shown in Figure 5(a). Following an initial increase in laser power, there was a notable increase in the vertical dimension (line height) of the graphene: from 77 μm to 150 μm. We ascribe this to the intensified degradation experienced by the PI film under higher laser powers, which consequently lead to the increased generation of graphene. There also exists a symmetric relationship between the horizontal dimension (line width) and the inter-line distance (line spacing) within the graphene structure. The sum of these two parameters remains constant at 110 μm, corresponding to a fixed line spacing value of 100 μm. The microstructure-change diagram (Figure 5(b)) shows that the laser power primarily affects the height rather than width of the graphene-wire arrays. Furthermore, the combination of SEM and LSCM test results shows that protruding lines are induced on the graphene by the concentrated Gaussian distribution of laser energy, while gaps within the array are formed due to heat accumulation during laser irradiation.

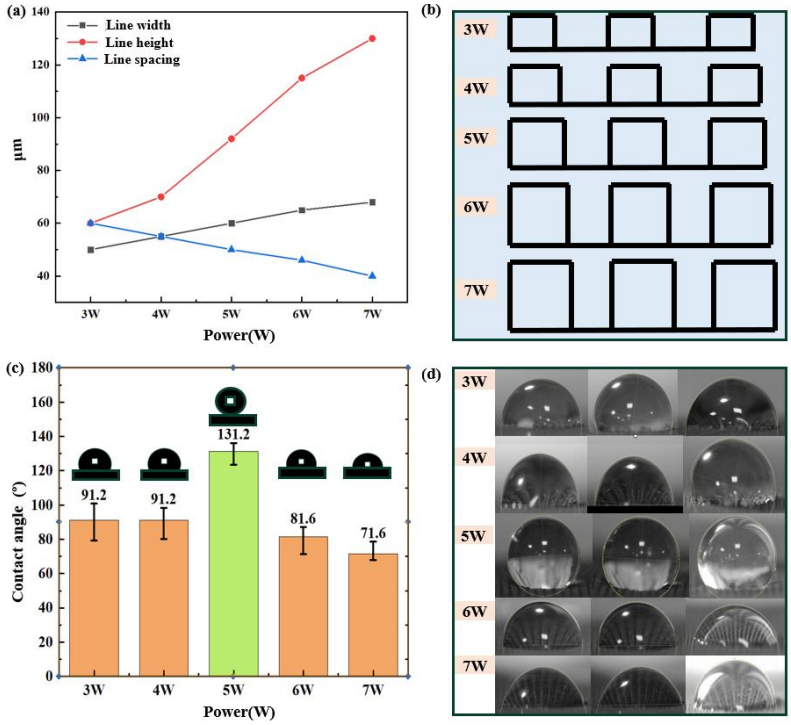

Figure 5 Hydrophobicity characterization. (a) Variations of line height, line width, and line spacing. (b) Schematic diagram of microstructure changes. (c) Relationship between water contact angle and laser power. (d) Real images of contact angles

To construct hydrophobic structures using a line array of graphene, we employed a contact-angle measuring instrument to evaluate the hydrophobicity of the graphene surface prepared at various power levels. The variations of, and real images depicting, water contact angles are presented in Figure 5(c) and (d). From the definition of wetting characteristics, a water droplet on a solid surface

Preprints.org (www.preprints.org) | NOT PEER-REVIEWED | Posted: 2 July 2024 doi:10.20944/preprints202407.0123.v1

is considered hydrophilic when the contact angle is CA < 90°, while a hydrophobic state is indicated by a contact angle CA > 90°. Furthermore, a superhydrophobic state can be inferred when the contact angle exceeds 150°. In terms of infiltrating properties, the graphene surface exhibits hydrophobic behavior over the range of laser powers from 3W to 5W, while it demonstrates hydrophilic characteristics at the laser-power levels of 6W and 7W. The microstructure-change diagrams show that lower powers (≤5 W) result in larger line spacings and narrower line widths, which provide a sufficient air cushioning structure that allows complete immersion of liquid into the graphene grooves at the solid–liquid interface. Conversely, higher powers (> 5W) lead to smaller line spacings, reducing the contact area between air pads and liquid, thereby weakening anti-wetting ability. We therefore consider a power level of 5W to be the most suitable of those included in this study for producing hydrophobic performance.

3.4 Electrical Conductivity of the LIG

Joule heating of the graphene surface is influenced by its resistance (or conductivity)[37]. We therefore utilized a four-probe resistance tester to measure the square resistance of the surface, as depicted in Figure 6(a). As shown in Figures 2 and 3, at the power levels of 3 W and 4 W the insufficient height and width of the graphene generated within the gaps in the graphene-line array, along with its overall inferior quality, can be attributed to the uneven accumulation of heat. Consequently, at these power levels, the square resistance of the graphene surface is only measured to be 23.7 kΩ and 17.5 kΩ, respectively. As the power is increased to 5 W or higher, the square resistance decreases significantly—to approximately 10 Ω—with a minimum value as low as 3.6 Ω. This demonstrates that the structures within the graphene-wire array possess sufficient height and width to enhance the electrical conductivity while also facilitating the enhancement of conductivity between the gaps.

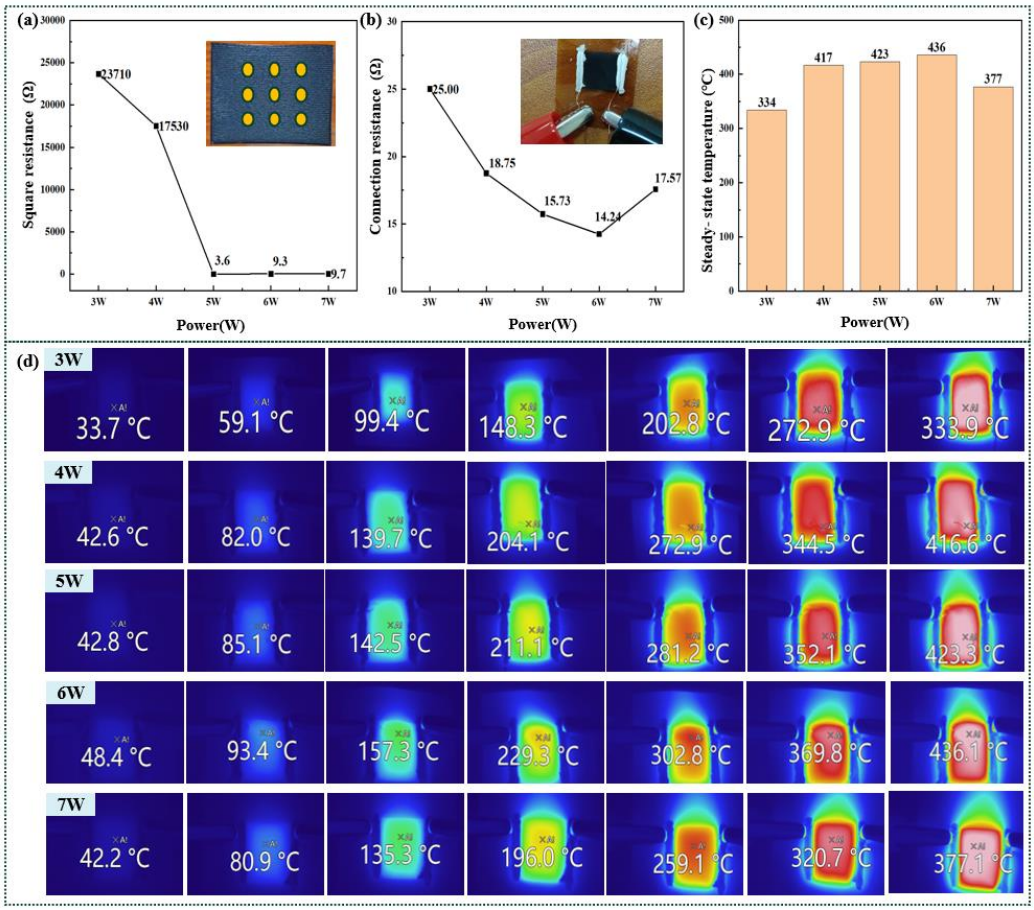

 doi:10.20944/preprints202407.0123.v1

Figure 6 Electrical conductivity characterization. (a) Square resistance. (b) Connection resistance. (c) Relationship between the Joule-heating steady-state temperature and laser power. (d) Infrared image of the steady-state temperature of the graphene surface produced by Joule heating.

After performing these tests and analyzing the square resistance of the graphene surface, we fabricated terminals to connect it to the programmable linear DC voltage-regulator power supply by applying a layer of conducting silver paste to both ends of the line array. We measured the current passing through the graphene by applying varying voltages to these terminals, and converted the results into connection resistances, as shown in Figure 6(b). For the power levels of 3 W and 4 W, we measured the connection resistances of the graphene surface to be 25 Ω and 18.75 Ω, respectively, which is significantly lower than their respective square resistances. We attributed this to complete connectivity of the entire structure of the wire arrays on the graphene surface, with conducting silver paste at both ends bridging any gaps within this wire-array structure. Consequently, the individual graphene wires are extended to form a continuous graphene surface. Furthermore, higher power levels lead to reduced connection resistances (ranging from 14.24 Ω to 25 Ω), indicating that increased laser power enhances the conductivity, resulting in a lower connection resistance of the graphene surface.

We further utilized an infrared thermal imager to monitor and record the Joule heating produced due to electrical heating of the graphene surface. The results of this Joule-heating steady-state temperature test of the graphene surface are shown in Figure 6(c), while the infrared thermal images of the electrical heating are presented in Figure 7(d). These results show that a decrease in the connection resistance corresponds to an increase in the steady-state temperature of the graphene surface, which is consistent with the relation $P = U^2/R$, where P is the power dissipated in the surface, U is the applied voltage, and R is the resistance. Moreover, by varying the power-supply voltages, it is feasible to adjust the temperature range of the graphene surface from 33.7°C to 436°C. However, because temperatures exceeding 400°C may lead to deformation or damage of the PI substrate film, we recommend that the stable electrothermal temperature of the graphene surface be lowered appropriately in subsequent work by adjusting other laser parameters or by modifying its mode of connection.

5. Conclusions

We have investigated the effects of laser power over the range 3–7 W, in intervals of 1W, on the surface structure and quality of graphene and have analyzed the hydrophobicity and electrothermal properties of the surface. Based on the experimental results, following conclusions were drawn:

Low laser powers (3–4 W) resulted in the formation of an uneven “sand-ridge” structure that overlapped on the graphene surface, accompanied by pores with larger apertures. High laser powers (6–7 W) led to increased decomposition of PI, which resulted in a higher density of surface defects characterized by pores with large aperture sizes. At a power level of 5 W, the graphene surface appeared flatter with smaller apertures. In general, the relationships between overall laser power and hole diameter and between laser power and roughness exhibited symmetrical distributions along the X-axis.

High laser powers (6–7 W) caused a decrease in the air content within gaps, leading to the development of hydrophilic surfaces. In contrast, low powers (3–4 W) promoted the formation of hydrophobic structures. Specifically, we observed the production of highly hydrophobic surfaces, with contact angles measuring CA = 131.2°, at a power level of 5 W. All graphene surfaces displayed low connection resistance and demonstrated excellent Joule-heating efficiency, confirming their potential application in electrothermal deicing systems. However, it is essential to adjust both the scanning speed and the voltage-connection mode appropriately to achieve an optimal steady-state temperature.

We obtained a hydrophobic graphene surface by using a well-designed patterning approach. By investigating the key factors affecting the morphology and quality of the graphene surface—

specifically, the laser power—we have established empirical relationships that govern its influence. Through a comparative analysis of the results, we have determined that a laser power of 5 W is optimal for achieving a hydrophobic graphene surface; however, further improvements are still required to enhance its hydrophobic characteristics. It is therefore necessary to analyze the effects of the laser-scanning speed and the line spacing of the periodic line array in order to achieve enhanced optimization and improvements of these characteristics.

Author Contributions: Conceptualization, methodology, software, validation, data curation and writing—original draft preparation, M.Z. and S.L.; resources, validation, formal analysis, H. F.; investigation H.Z.; visualization, Y.J.; data curation, J.L.; supervision writing—review and editing and funding acquisition, L.Y. All authors have read and agreed to the published version of the manuscript.

Funding: The authors gratefully acknowledge the financial support from the Key Laboratory of Flight Techniques and Flight Safety, CAAC(FZ2022ZZ03), the General Project of Sichuan General Aircraft Maintenance Engineering and Technology Research Center (GAMRC2021YB12), the National Natural Science Foundation of China (52205238), and Chongqing Natural Science Foundation Innovation and Development Joint Fund(CSTB2022NSCQ-LZX0080).

Institutional Review Board Statement: Not applicable.

Informed Consent Statement: Not applicable.

Data Availability Statement: Data sharing is not applicable to this article.

Acknowledgments: Not applicable.

Conflicts of Interest: The authors declare no conflict of interest.

Reference

1. He Q, Li K, Xu Z, et al. Research progress on construction strategy and technical evaluation of aircraft icing accretion protection system. *Chinese J Aeronaut*, 2023, 36(10):1-23.
2. Zhu C, Zhu C. Aircraft icing and its protection. Beijing: Science Press, 2016.
3. Liu Y, Wu Y, Ma Y, et al. Reversible thermochromic and heat storage coating for adaptive de/anti-icing and thermal regulation[J]. *Chem Eng J*, 2024, 482: 148837.
4. Zhang S, Gao F, Jiang Z, et al. Bioinspired durable interpenetrating network anti-icing coatings enabled by binders and hydrophobic-ion specific synergies. *Chem Eng J*, 2024, 479: 147836.
5. Xue Y, Wang Y, Wang Y, et al. A superhydrophobic Fe3O4/PEI nanocomposite film with active activation function for anti-icing/deicing applications. *Mater Today Sustain*, 2023, 24:100588.
6. Chen L, Xu J, Luo X, et al. Micro/nano manufacturing aircraft surface with anti-icing and deicing performances: An overview. *Nanotechnol Rev*, 2023, 12(1): 20230105.
7. Wu H, Shi F, Zhang Z, et al. Effect of carbon fiber bundles spacing on composites and their electro-thermal and anti/deicing properties. *Mat Sci Eng B-ADV*, 2024, 299: 117021.
8. Zhang W, Wang D, Sun Z, et al. Robust super hydrophobicity: mechanisms and strategies. *Chem Soc Rev*, 2021, 50(6): 4031-4061.
9. Liu S, Wang Y, Tang X, et al. Fabrication of polydimethylsiloxane superhydrophobic coatings with self-healing properties using the template method. *J Mater Eng Perform*, 2024, 33, 1349–1357.
10. Pan R, Zhong M L. Fabrication of superwetting surfaces by ultrafast lasers and mechanical durability of superhydrophobic surfaces. *Chin Sci Bull*, 2019, 64(12): 1268-1289.
11. Li Z, Zhen Z, Chai M, et al. Transparent electrothermal film defoggers and antiicing coatings based on wrinkled graphene. *Small*, 2020, 16(4): 1905945.
12. Xiao Z, Chen C, Liu S, et al. Endowing durable icephobicity by combination of a rough powder coating and a superamphiphobic coating. *Chem Eng J*, 2024, 482: 149001.
13. Zhang R, Ding Z, Wang K, et al. Enhanced anti/de-icing performance on rough surfaces based on the synergistic effect of fluorinated resin and embedded graphene. *Small Methods*, 2024, 1:2301262.
14. Zhang B, Yang G, Xu W, et al. Hybrid superamphiphobic anti-corrosion coating with integrated functionalities of liquid repellency, self-cleaning, and anti-icing. *J Mater Sci Technol*, 2024, 184: 256-268.
15. Chen Q, Shen X, Zhang Z, et al. Robust superhydrophobic SiO2/GPE/MWCNTs durable composite coating with photothermal and electrothermal effect for passive anti-icing/active de-icing. *Prog Org Coat*, 2024, 191: 108438.
16. Zhao Z, Chen H, Zhu Y, et al. A robust superhydrophobic anti-icing/de-icing composite coating with electrothermal and auxiliary photothermal performances. *Comp Sci Technol*, 2022, 227: 109578.

17. Hou Y, Wang M, Choy K L. Scalable high-efficiency multilayered anti-icing/de-icing coating: Superhydrophobic upper layer boosts the performance of the electrothermal system. *Prog Org Coat*, 2022, 168: 106866.
18. Fan J, Long Z, Wu J, et al. Electrothermal superhydrophobic epoxy nanocomposite coating for anti-icing/deicing. *J Coat Technol Res*, 2023, 20(5): 1557-1568.
19. Duy L X, Peng Z, Li Y, et al. Laser-induced graphene fibers[J]. *Carbon*, 2018, 126: 472-479.
20. Ye R, James D K, Tour J M. Laser-induced graphene. *Accounts Chem Res*, 2018, 51(7): 1609-1620.
21. Kim K Y, Choi H, Van Tran C, et al. Simultaneous densification and nitrogen doping of laser-induced graphene by duplicated pyrolysis for supercapacitor applications. *J Power Sources*, 2019, 441: 227199.
22. Li Y L, Luong D X, Zhang J B, et al. Laser-induced graphene in controlled atmospheres: from superhydrophilic to superhydrophobic surfaces. *Adv Mater*, 2017, 29(27): 1700496.
23. Tittle C M, Yilman D, Pope M A, et al. Robust superhydrophobic laser-induced graphene for desalination applications. *Adv Mater Technol*, 2018, 3(2): 1700207.
24. Nasser J, Lin J, Zhang L, et al. Laser induced graphene printing of spatially controlled super-hydrophobic/hydrophilic surfaces. *Carbon*, 2020, 162: 570-578.
25. Lee J U, Lee C W, Cho S C, et al. Laser-induced graphene heater pad for de-icing. *Nanomaterials*, 2021, 11(11): 3093.
26. Deshmukh S, Banerjee D, Quintero J S M, et al. Polarity dependent electrowetting for directional transport of water through patterned superhydrophobic laser induced graphene fibers. *Carbon*, 2021, 182: 605-614.
27. Han Y, Han Y, Sun J, et al. Controllable nanoparticle aggregation through a superhydrophobic laser-induced graphene dynamic system for surface-enhanced Raman scattering detection. *ACS Appl Mater Interfaces*, 2022, 14(2): 3504-3514.
28. Wu W, Liang R, Lu L, et al. Preparation of superhydrophobic laser-induced graphene using taro leaf structure as templates. *Surf Coat Tech*, 2020, 393: 125744.
29. Wang W, Lu L, Lu X, et al. Laser-induced jigsaw-like graphene structure inspired by Oxalis corniculata Linn. leaf. *Bio-Des Manuf*, 2022, 5(4): 700-713.
30. He Q, Ma Y, Wang X, et al. Superhydrophobic flexible silicone rubber with stable performance, anti-icing, and multilevel rough structure. *ACS Appl Poly Mater*, 2023, 5(7): 4729-4737.
31. Li A, Wei Z, Zhang F, et al. A high reliability super hydrophobic silicone rubber. *Colloid Surface A*, 2023, 671: 131639.
32. Li S, Zhong M, Zou Y, et al. Fabrication of micron-structured heatable graphene hydrophobic surfaces for deicing and anti-icing by laser direct writing[J]. *Coatings*, 2023, 13(9): 1559.
33. Zhong M, Li S C, Zou Y, et al. Hydrophobic surface array structure based on laser-induced graphene for deicing and anti-icing application. *Micromachines*, 2024, 15(2):285.
34. He Q, Xu Y, Zhang F, et al. Preparation methods and research progress of super-hydrophobic anti-icing surface[J]. *Adv Colloid Interface Sci*, 2023: 103069.
35. Han Y, Han Y, Huang Y, et al. Laser-induced graphene superhydrophobic surface transition from pinning to rolling for multiple applications. *Small Methods*, 2022, 6(4): 2200096.
36. Wang Y, Wang Y, Zhang P, et al. Laser-induced freestanding graphene papers: A new route of scalable fabrication with tunable morphologies and properties for multifunctional devices and structures. *Small*, 2018, 14(36): 1802350.
37. Jia Y, He Q, Liu Y, et al. Anti-icing system based on multi-level micro-nano and electric heating dual structure[J]. *Colloid Surface A*, 2024, 683: 133105.